Research Square

Preprints are preliminary reports that have not undergone peer review.
They should not be considered conclusive, used to inform clinical practice,
or referenced by the media as validated information.

Ventilation of a Single-Entrance Cave by Buoyancy-Driven Exchange Flow

Franci Gabrovšek

franci.gabrovsek@zrc-sazu.si

Research Centre of the Slovenian Academy of Sciences and Arts

Vanessa E. Johnston

Research Centre of the Slovenian Academy of Sciences and Arts

Nenad Buzjak

University of Zagreb

Dalibor Paar

University of Zagreb

Matej Blatnik

Research Centre of the Slovenian Academy of Sciences and Arts

Andrea Martín Pérez

Research Centre of the Slovenian Academy of Sciences and Arts

Article

Keywords: Cave microclimate, Exchange flow, Density-driven flow, Natural ventilation

Posted Date: November 9th, 2026

DOI: https://doi.org/10.21203/rs.3.rs-11381623/v1

License: This work is licensed under a Creative Commons Attribution 4.0 International License.
Read Full License

Additional Declarations: No competing interests reported.

Ventilation of a Single-Entrance Cave by Buoyancy-Driven Exchange Flow

Franci Gabrovšek[1,*] • Vanessa E. Johnston [1] • Nenad Buzjak[2] • Dalibor Paar[3] • Matej Blatnik[1] • Andrea Martín-Pérez[4]

***Corresponding author: Franci Gabrovšek, franci.gabrovsek@zrc-sazu.si**

Abstract

Karst caves are unique subsurface environments in which climate is governed by the interplay between advective heat transport by airflow, convective heat exchange at the rock–air interface, and conductive heat transport within the surrounding rock. Airflow is a major driver of heat and CO_2 exchange between the cave environment and the atmosphere, yet the physical mechanisms controlling cave ventilation across different morphologies and timescales remain poorly understood. We investigate temperature and airflow in a single-entrance cave consisting of a dominant down-sloping passage connected to a set of chambers. Such caves exhibit buoyancy-driven ventilation during cold periods, when dense external air descends along the floor of the entrance passage while warmer cave air ascends along the ceiling as a bidirectional counterflow. During warm periods, ventilation is largely suppressed and cave temperatures gradually equilibrate. Airflow and temperature observations reveal a buoyancy-driven exchange flow governed by heat transfer with the surrounding rock and sediments and mixing between the opposing layers. Cooling of the rock and sediments during cold-air intrusions prolongs ventilation and modifies the response to subsequent cooling events. Thus, ventilation depends on both the instantaneous cave–atmosphere temperature difference and the thermal history of the surrounding rock and sediments.

✉ Franci Gabrovšek franci.gabrovsek@zrc-sazu.si

[1] Karst Research Institute, ZRC SAZU, Postojna, 6230, Slovenia

[2] Department of Geography, Faculty of Science, University of Zagreb, Zagreb, Croatia

[3] Department of Physics, Faculty of Science, University of Zagreb, Zagreb, Croatia

[4] Ivan Rakovec Institute of Palaeontology, ZRC SAZU, 1000, Ljubljana, Slovenia

Keywords Cave microclimate · Exchange flow · Density-driven flow · Natural ventilation

1 Introduction

Karst areas, which cover approximately 15% of the Earth's ice-free land surface, represent a unique interface through which surface hydrological and meteorological signals penetrate deep into the subsurface (D. C. Ford and Williams 2007; Covington et al. 2012). The karst subsurface is usually not isolated from the external atmosphere but is connected to it through conduits and fracture networks of various sizes that permit substantial water and air flow. The transport of heat and mass through karstified structures plays a crucial role in the physical, chemical, and biological processes that drive karst evolution and sustain the ecological functioning of karst landscapes (Luhmann et al. 2015). Understanding these transport processes is important not only for karst research but also for evaluating the contribution of karst areas to the global carbon budget.

Airflow through conduits and dissolutionally enlarged fracture networks plays an important role in the thermal regime of karst massifs and in the transport of gases, particularly CO_2, thereby influencing carbonate dissolution and precipitation (Kowalczk and Froelich 2010; Kukuljan et al. 2021; Spotl et al. 2005). Airflow through karst massifs is primarily driven by buoyancy forces, external pressure changes, and groundwater movement (Badino 1995; Palmer 2007; J. D. Ford and Cullingford 1976). The dominant driver of buoyancy-driven airflow is the temperature difference between the external atmosphere and the cave air, which is largely controlled by heat exchange between the air and the surrounding rock massif (Lismonde 2002). Consequently, the chimney effect is the dominant ventilation mechanism in caves with multiple connections to the surface at different elevations. In general, the chimney effect drives airflow from lower to higher entrances during cold periods and in the opposite direction during warm periods. However, the geometrical complexity of cave and fracture systems gives rise to intricate ventilation patterns that are still not fully understood (Gabrovšek 2023). In relatively uniform passages, chimney-driven ventilation is approximately symmetric: for the same temperature difference between the external atmosphere and the cave, the magnitude of the upward airflow during winter is similar to that of the downward airflow during summer. However, even a single passage connecting two entrances may exhibit asymmetric ventilation if its

longitudinal profile or cross-section is non-uniform. In such cases, upward or downward airflow may dominate under the same external forcing. Extreme examples are V-shaped and Λ-shaped passages (i.e. systems with two entrances at the same or similar elevation and a connecting passage lying below or above them, respectively), where ventilation may be restricted almost exclusively to cold or warm periods, respectively (Gabrovšek 2023; Lismonde 2002).

Caves with a single entrance represent another end-member case of asymmetric ventilation. If such systems are ventilated, air must both enter and leave the cave through the same passage, leading to the formation of a bidirectional counterflow. In a down-sloping passage during cold periods, dense external air flows inward along the lower part of the passage, while warmer less-dense cave air flows outward along the upper part. During warm periods, ventilation is largely suppressed. By contrast, in an up-sloping passage the situation is reversed.

The seasonal filtering of ventilation, whereby exchange with the external atmosphere is restricted predominantly to either cold or warm periods, gives rise to so-called cold and warm traps (Luetscher et al. 2008; Šebela and Turk 2018). These natural thermal traps have long been exploited by humans for winter shelter (Mihevc 2018), ice harvesting (Mihevc 2021), and food storage. Cold traps are also the most favorable environments for the development of perennial cave ice because their mean internal temperature remains significantly below the mean annual temperature of the external atmosphere (Perşoiu and Onac 2012; *Ice Caves* 2018).

The buoyancy-driven counterflow observed in single-entrance caves is closely related to the classical ventilation problem of a room with a single window (Linden 1999). Opening a window to a colder external atmosphere induces the intrusion of dense outside air, mixing within the room, and the simultaneous outflow of warmer indoor air through the same opening. Similar counterflows have also been studied extensively in fluid mechanics because of their importance in geophysical fluid dynamics, oceanic overflows, atmospheric motions, and building ventilation (Meyer and Linden 2014; Lefauve and Linden 2022; Armi 1986).

Despite their abundance, ventilation in single-entrance caves has received far less attention than chimney-effect ventilation, and the physical mechanisms controlling buoyancy-driven counterflow and heat transfer in such systems remain poorly understood (Lismonde 2002). In this work, we present airflow and temperature observations from the single-entrance Koželevka Cave in the Dinaric karst of Slovenia. The cave was selected because of its extensive moonmilk deposits, whose formation remains poorly understood (Miller et al. 2018; Ghezzi et al. 2024) and may be linked to cave microclimate (Borsato et al. 2000; Lacanette et al. 2023). Initial observations revealed complex ventilation dynamics, motivating progressively more detailed measurements and a dedicated investigation of the cave's airflow and thermal regime. We interpret the observed airflow and temperature patterns within the framework of buoyancy-driven counterflow maintained by heat transfer between the air, the surrounding rock, and cave sediments.

2 Study site and methods

Koželevka Cave is 130 meters long and 42 meters deep, with its entrance located at an elevation of 630 meters above sea level. The cave is a fragment of a partially degraded and collapsed fossil conduit in the hinterland of Ljubljanica River karst springs, situated about 330 meters above the present level of regional karst springs (Fig. 1).

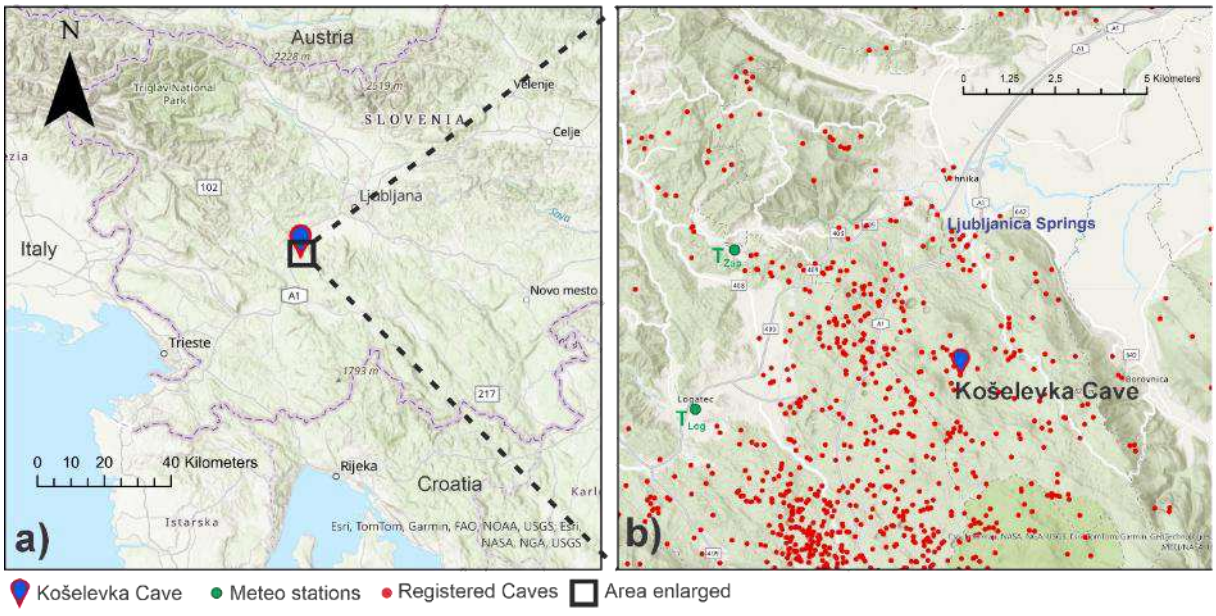


Fig. 1 Geographic location of Koželevka Cave. (a) Regional setting. (b) Enlarged map showing the locations of cave entrances and meteorological stations. T_{Log} and T_{Zap} indicate the Logatec and Zaplana meteorological

stations, respectively, whose records were used as references for external air temperature during the 2021–2022 monitoring period.

The cave (Fig. 2) features an opening of 6 m x 2 m, leading to a 60 m long downward inclined passage. This passage opens into a larger chamber, from which a partially collapsed corridor leads to a smaller, dead-end chamber. Two other dead-end passages descend from the main chamber. Additionally, two vertical passages diverge from a side niche of the main chamber, but they become impassable after a few tens of meters. The cave walls are partially covered by speleothems, either in the form of crystalline flowstone and dry or water-saturated moonmilk (i.e., fibrous microcrystalline calcite). The cave floor is covered by a mixture of limestone debris of various sizes, ranging from blocks exceeding one meter in size to cobbles, sand, and fine silt-sized cave sediments.

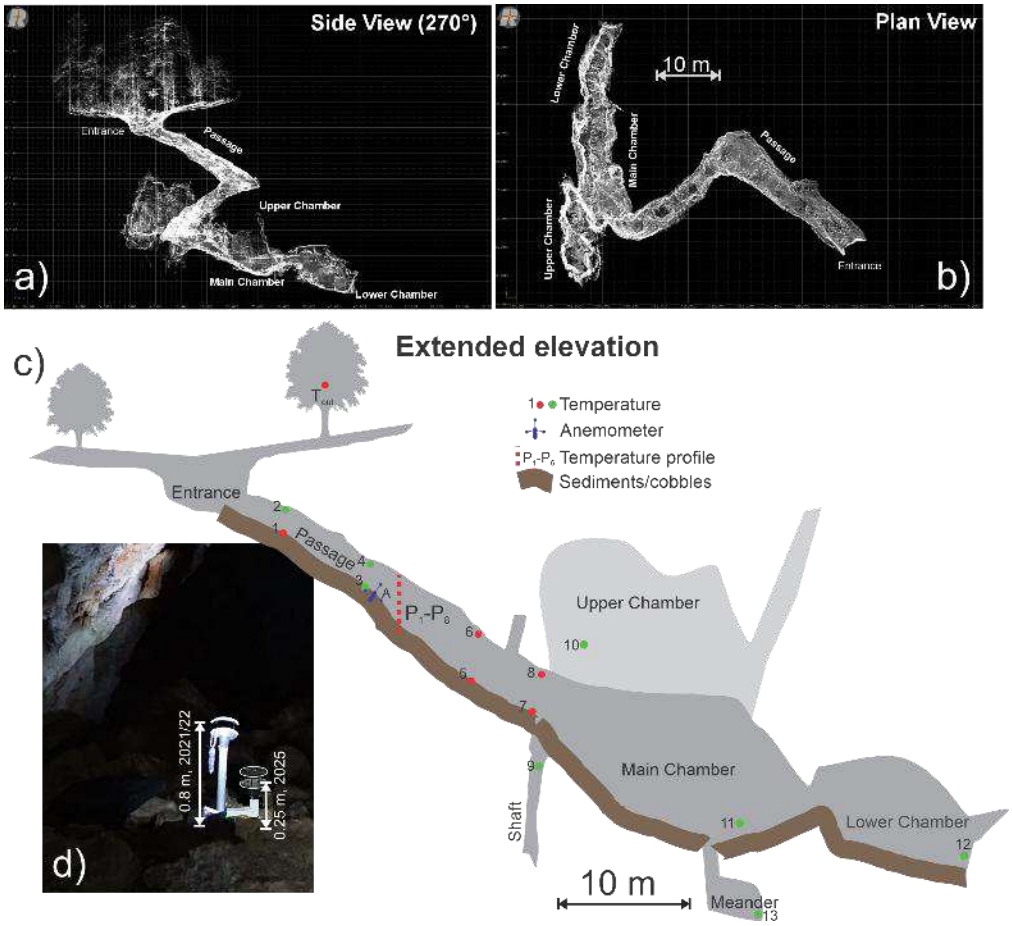


Fig. 2 Cave geometry and monitoring locations. (a) Cross-section of the point cloud acquired with a RIEGL VZ-2000i terrestrial laser scanner. (b) Plan view of the point cloud. (c) Simplified cross-section showing the monitoring locations. Points 1–13 indicate temperature-loggers inside the cave; green symbols denote loggers operating also during the 2021/22 monitoring period, and red symbols denote additional loggers deployed

during 2025/26. T_{out} indicates the external temperature logger deployed near the cave entrance during the 2025/26 campaign. P1–P8 indicate the positions of the loggers used to measure the vertical temperature profile in January 2026. (d) Anemometer positions during the 2021/22 and 2025/26 monitoring periods.

2.1 Local climate

The climate is temperate continental (Köppen Cfb). Winters are cold, with nighttime temperatures frequently dropping below freezing. The number of cold days ($T_{min} < 0$ °C) is around 100 per year in the 2020s, with about 10 fully frozen days ($T_{max} < 0$ °C). Extreme winter minima can fall below −20 °C. Summers are warm to occasionally hot, with daytime highs reaching up to 30 °C, accompanied by cooler nights. The mean annual temperature in nearby Logatec meteorological station (Fig. 1) for the period 1991–2020 was 8.8 °C, with a clear warming trend of approximately 0.33 °C per decade. In the 2020s, the annual mean has risen to about 10 °C. Precipitation is evenly distributed throughout the year, with a peak in autumn, totaling roughly 1800 mm annually. The number of days with snow cover (>1 cm) shows a decreasing trend (−6 days per decade) and is currently around 30 days per year.

2.2. Methods

Temperature was measured using HOBO TidbiT MX Temp 400 temperature data loggers (MX2203; Onset Computer Corporation, USA), with an accuracy of ±0.2 °C between 0 and 70 °C, ±0.25 °C between −20 and 0 °C, and a resolution of 0.01 °C. Before deployment, the temperature loggers were cross-calibrated in a thermostatically controlled chamber, and systematic inter-instrument offsets were corrected during post-processing. Temperature was recorded at 10-minute intervals unless stated otherwise.

Airflow was measured using a Gill WindSonic Option 1 two-axis ultrasonic anemometer with RS232 output (Gill Instruments, UK). The instrument has a starting threshold and resolution of 0.01 m s^{-1} and a stated accuracy of 2% RMSE at 12 m s^{-1}. Airflow was sampled at either 1 or 0.25 Hz. The measurements were aggregated into 10-minute intervals, for which the mean (v_{av}) and maximum (v_{max}) airflow velocities were calculated.

Although temperature was monitored continuously at several locations from autumn 2021 to autumn 2025 (Fig. 3), simultaneous temperature and airflow measurements were concentrated in two principal campaigns: autumn 2021 to spring 2022 and autumn–winter

2025/26. During the 2025/26 campaign, additional MX2203 loggers were installed along the cave passage (Fig. 2). External air temperature during the 2025/26 campaign was measured using a radiation-shielded MX2203 logger installed immediately above the cave entrance. Between 18 and 31 January 2026, a vertical temperature profile was recorded using eight MX2203 loggers positioned at different heights above the passage floor (Fig. 2c).

Before installation of the local external logger, regional external-temperature variability was represented by records from the Zaplana meteorological station and Logatec meteorological station (Fig. 3). These data were used only to provide temporal context for the long-term cave-temperature record. During the overlapping period from 10 to 23 November 2025, the local and Zaplana temperature records were strongly correlated ($r = 0.992$). The local temperature was, on average, 0.43 °C lower, with a mean absolute difference of 0.67 °C and an RMSE of 0.88°C. The Zaplana record was therefore considered adequate for illustrating regional external-temperature variability.

The main text focuses on the more detailed 2025/26 campaign, with supporting results from the 2021/22 campaign presented in the Supplementary Information.

During the 2021/22 campaign, the anemometer was installed about 0.8 m above the floor, while in 2025/26 it was installed at the same location on a shorter mast, about 0.25 m above the floor (Fig. 2d).

Airflow direction was also visualized qualitatively using commercially available incense sticks. Smoke observations were conducted throughout the cave and at several heights within the entrance passage to identify the presence and direction of airflow and the approximate position of the interface between the counterflowing layers (Fig. 3b). These observations informed the placement of the monitoring instruments but were not used to obtain quantitative airflow velocities.

3 Results

Fig. 3a shows the temperature at different locations within the cave and the external temperature at the Zaplana meteorological station (Fig. 1) between October 2021 and July 2024. The record shows episodes of cold air intrusions during the winter period, and asymptotic behavior, with temperatures approaching an equilibrium value (in the case of Košelevka, about 7.5 °C) between spring and autumn. Such temperature patterns are

common and typical of caves with a single opening to the surface and a negligible chimney effect, as well as in V-shaped caves (i.e., caves with two entrances at similar elevations) (Gabrovšek 2023; Ravbar et al. 2014; Šebela and Turk 2018; Buzjak et al. 2024; Luetscher et al. 2005). In these caves, a strong ventilation regime occurs during cold periods, while ventilation is minimal or nearly absent in summer. Good qualitative information about the spot ventilation pattern can be obtained using smoke sticks. Fig. 3b shows airflow directions at an external temperature of −1 °C, obtained using a simple method in which incense sticks were fixed to a rod at different elevations above the ground, about 20 m below the entrance in the downward sloping passage. The results show strong downward airflow into the cave in the lower part of the passage (at 0.3 m above the floor), with a returning upward flow in the upper part of the passage (1.5 and 2 m high), and changing direction in the middle section (1 m-high). From here on, we use *upflow* for air moving upward along the ceiling section of the channel, and *downflow* for airflow descending along the floor section. Videos of the smoke-stick observations are available in the data repository (Gabrovšek 2026).

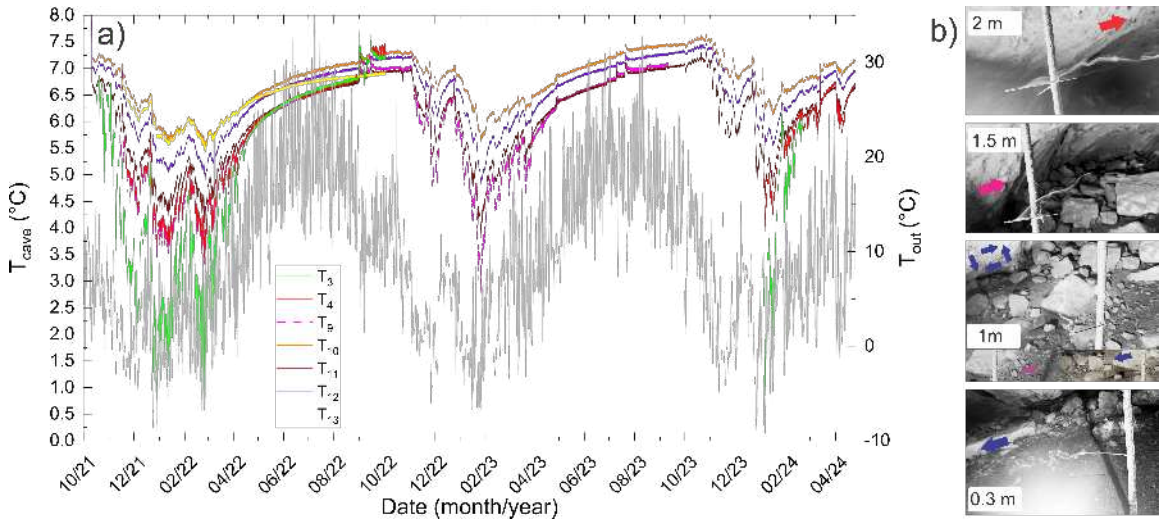


Fig. 3 a) Temperature records at different sites (see Fig. 2) in Koševelka (T_{cave}) and external temperature at Zaplana weather station (T_{out}). b) Smoking sticks indicating airflow at different heights above the floor during cold air intrusion in January 2026. The location of photos is in the inclined passage, about 20 m from the entrance; entrance is to the right.

We now turn to detailed observations in late autumn, 2025. Fig. 4 presents time series data of airflow, temperatures at points 3 and 4 in the cave, the temperature difference between

these two points, and the outside temperature from 9 November to 11 December 2025. The anemometer was positioned in the lower section of the channel, about 25 cm above the floor at point 3 (Fig. 2). At this point, the airflow for the entire period is directed into the cave along the downward-sloping floor (downflow), as observed by smoke sticks (see Fig. 3b).

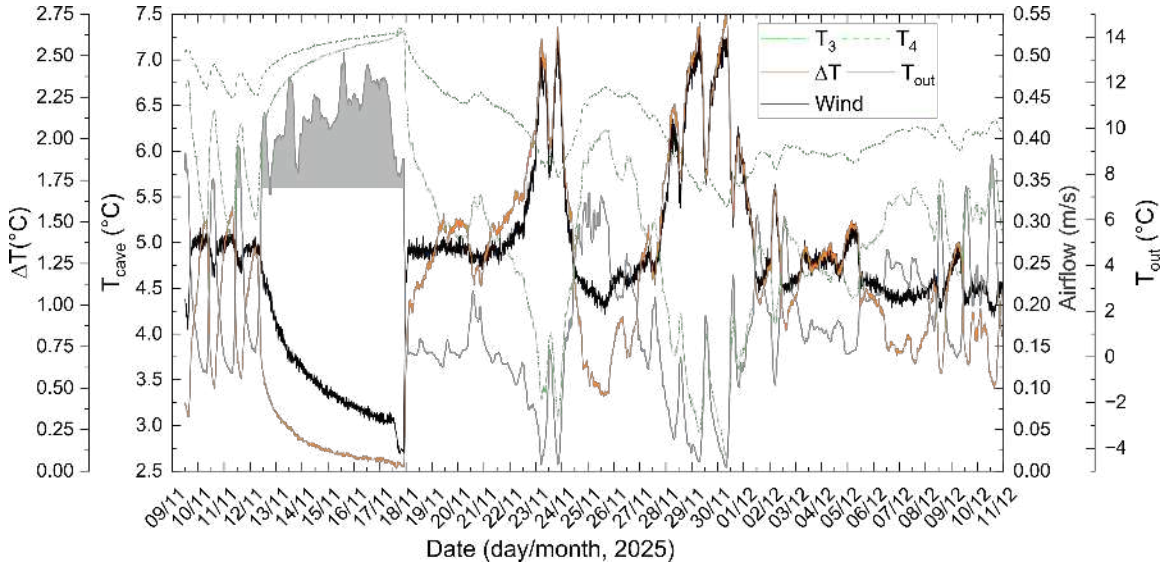


Fig. 4 Cave microclimate in November–December 2025. External temperature, airflow velocity and temperature 0.25 m above the floor (Point 3 on Fig. 2) and 0.2 m below the ceiling (T_4) of the inclined passage, and temperature difference between points 4 and 3 ($\Delta T = T_4 - T_3$). Shaded region marks the period when external temperature was above 7.5 °C.

In Fig. 4, the initial period (9 November to 11 November 2025) was characterized by stable autumn weather with a pronounced diurnal temperature cycle, featuring daytime maxima between 7 °C and 9 °C and night-time minima just below the freezing point. The airflow remained relatively stable during the night and decreased only moderately during the day, when the external temperature rose.

On 12 November 2025, the outside temperature rose above 7.5 °C, when the airflow in the cave began to diminish with a time constant of approximately 1.5 days (approximating the relaxation by assuming exponential decay). Temperatures behaved asymptotically, differences between them diminished, and they both approached 7.5 °C. The temperature inside the cave (see also Fig. 5) was no longer affected by external temperature variations.

This indicates that intrusions of external cold air are limited to situations when the outside temperature falls below 7.5 °C, which we refer to as the switch temperature (T_{sw}). The grey area below the T_{out} curve denotes period when $T_{out} > T_{SW}$.

In the night between 17 and 18 November, the outside temperature dropped from 8.5 °C to just above 0 °C within three hours, triggering a rapid intrusion of cold air, as observed by the anemometer as an increase in airflow velocity and the temperature loggers recorded the cooling of cave air. Notably, the airflow velocity was similar to that during the initial stable autumn period (around 0.25 m/s) (Fig. 4).

During the remainder of the monitoring period (until 11 December 2025), the external temperature remained below the T_{sw}, reaching a minimum of −4.7 °C with the 10 min average airflow velocity (v_{av}) reaching maxima around 0.5 m/s. As expected, the airflow velocity is positively correlated with difference between the temperature below the ceiling and above the floor, $\Delta T = T_4 - T_3$. However, as it can be seen, and we demonstrate later, the relation between the two is far from linear. Several similar events recorded during the 2021/22 monitoring period are presented in the Supplementary Information (Fig. S1).

3.1 Temperature distribution along the passage and across the airflow layers

Fig. 5a shows temperature records along the floor of the cave (points 1,3,5,7,11) in Autumn 2025 period. Downflow temperature increases rapidly in the initial section (from 1 to 3), after which the rate of increase diminishes along the flow path (from 3 to 11). Along the cave ceiling (Fig. 5b), the upflow temperature decreases from point 8 toward the exit, with the smallest difference observed between points 6 and 4, and highest differences in the entrance part. In the inner part of the cave (Fig. 5c), the highest temperature was observed in the upper chamber (10) but this was similar to the deepest location in the cave (12). The temperature in the shaft (9) was close to temperature at point 7, the nearest temperature logger to point 9 in the downflow part of the inclined passage (Figs. 2 and 5c). Fig. 5d show temperature differences along consecutive points of the flow path. The differences are highest in the entrance part (T_3-T_1 and T_4-T_2) and during cold periods.

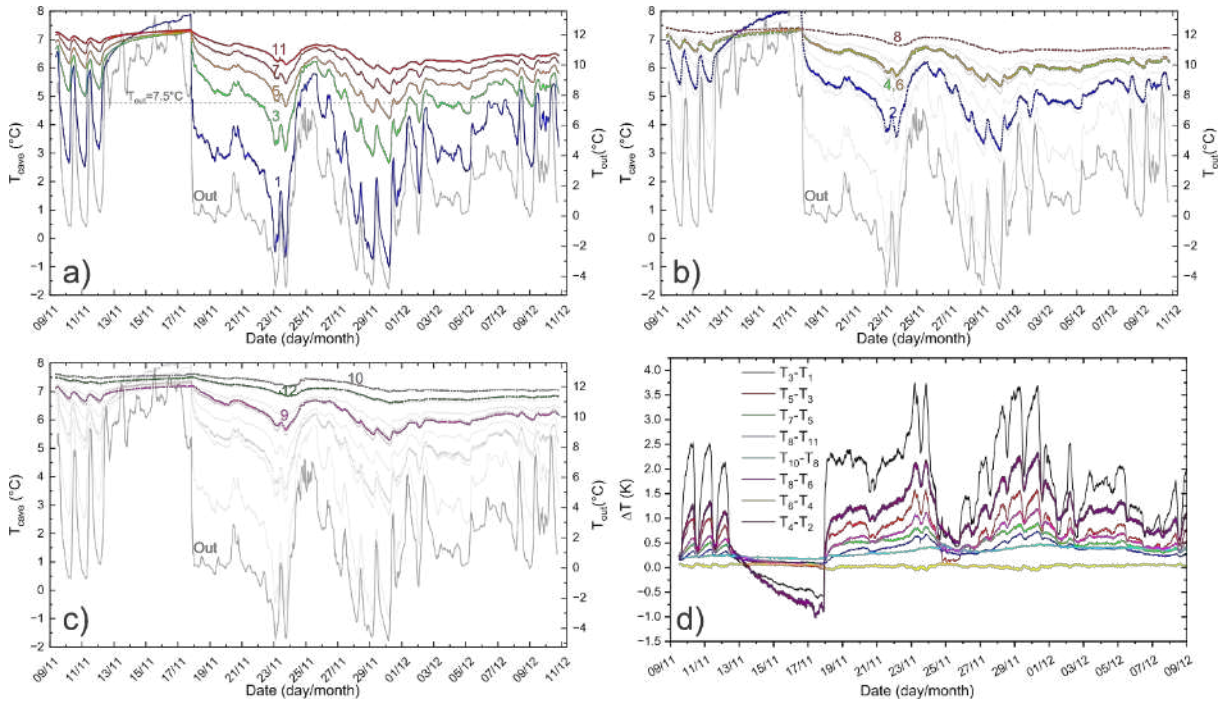


Fig. 5 Temperatures at different locations along the cave passage in autumn 2025. Time series of temperature along the downflow (a), upflow (b) and in the internal part of the cave (c). (d) Temperature differences between successive points along the flowpath (see Fig. 2 for locations). T_{out} and T_{cave} are at the different scales in panels a-c. In (b) and (c), the temperatures at all locations are shown as faint lines for reference.

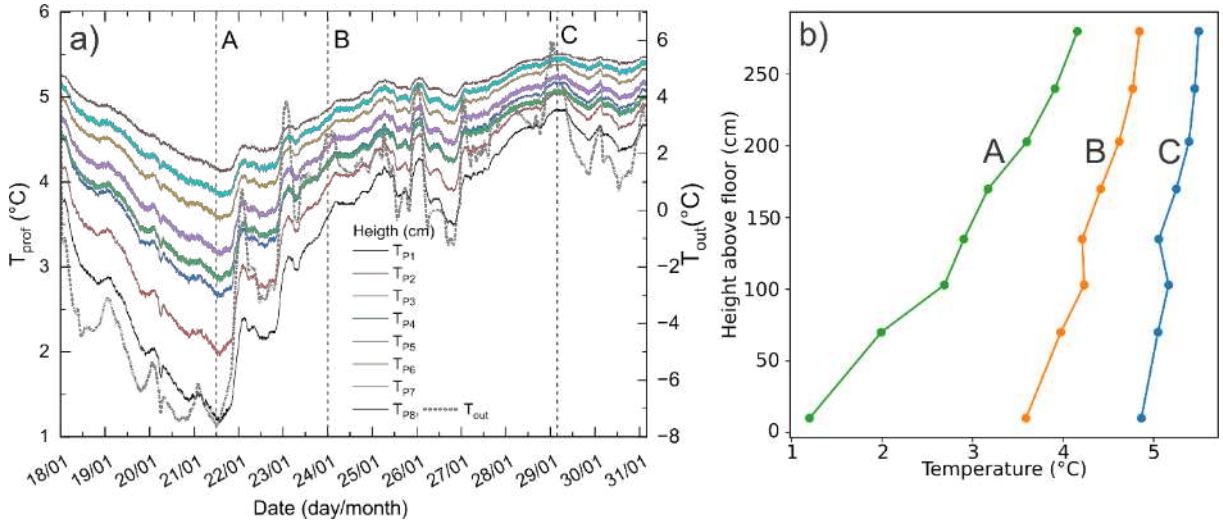


Fig. 6: Vertical temperature profile at point 3: a) Temperature records at different heights along profile P1–P8 (see Fig. 2) from 18 to 31 January 2026. b) Characteristic temperature profiles; see dashed lines in (a) for times of when the profiles were extracted.

Fig. 6a shows the temperature at different heights above the passage floor in January 2026 (at P1–P8 in Fig. 2). Fig. 6b shows temperature profiles at three selected times with

different T_{out} (-7.7°C (A), 2.6°C (B) and 5.5°C (C)) as marked in Fig. 6a. Overall, the temperature increases from the cave floor toward the ceiling (Fig. 6b). The gradient is highest during the coldest period (green line) and flattens as the system approaches the switch temperature (blue line). All three profiles also show a smaller vertical temperature gradient between 1.0 and 1.3 m above the cave floor.

Although CO_2 dynamics were not a primary focus of this study, sporadic measurements showed an apparent bimodal distribution, with concentrations of approximately 2,000 ppm during summer conditions with little or no airflow and 400–500 ppm during ventilated periods (Supplementary Information Fig. S2).

4 Discussion

The temperature and airflow records indicate that the intrusion of cold air is limited to periods during which the external temperatures (T_{out}) are below the switch temperature (T_{SW}), which in the case of Koševelka Cave was found to be close to 7.5°C, for the shown period (Fig. 4). To elucidate these relations, Fig. 7a shows airflow velocity as a function of the difference between the external and switch temperatures (T_{sw}-T_{out}) for the autumn 2025 period (as in Figs. 4 and 5). Colors indicate the position in time as the number of days from 9 November; see Fig. 7b inset graph with color coded line. When $T_n<0$, the airflow and external temperature are uncorrelated (left from the vertical dotted line). The decrease of airflow in the orange-yellow region (recession period; 12–17 November) was independent of the changes of external temperatures while they remained above T_{sw}. Yellow dots show the last part of the warm period where the airflow diminishes (17 November), and the subsequent cooldown on 18 November, when airflow increased vigorously due to the rapid drop in external temperature. Before the cooldown, the cave temperatures were approaching 7.5 °C (T_{sw}) and the airflow velocity approached zero (Fig. 4). Immediately on the rapid drop of external temperature, the initial increase of airflow was fast and lasted for about an hour (widely spaced yellow dots in Fig. 7a and Fig. 7b). A notable observation is that, apart from the initial rise in airflow velocity during rapid cooling, the airflow changes slowly with temperature for T_{sw} - T_{out} <7°C but with a further drop of external temperatures the slope increases. Furthermore, the relation between airflow and

temperature difference also changes in time; in the earlier period (red), the velocity is slightly higher than in the latter period for the same temperature difference.

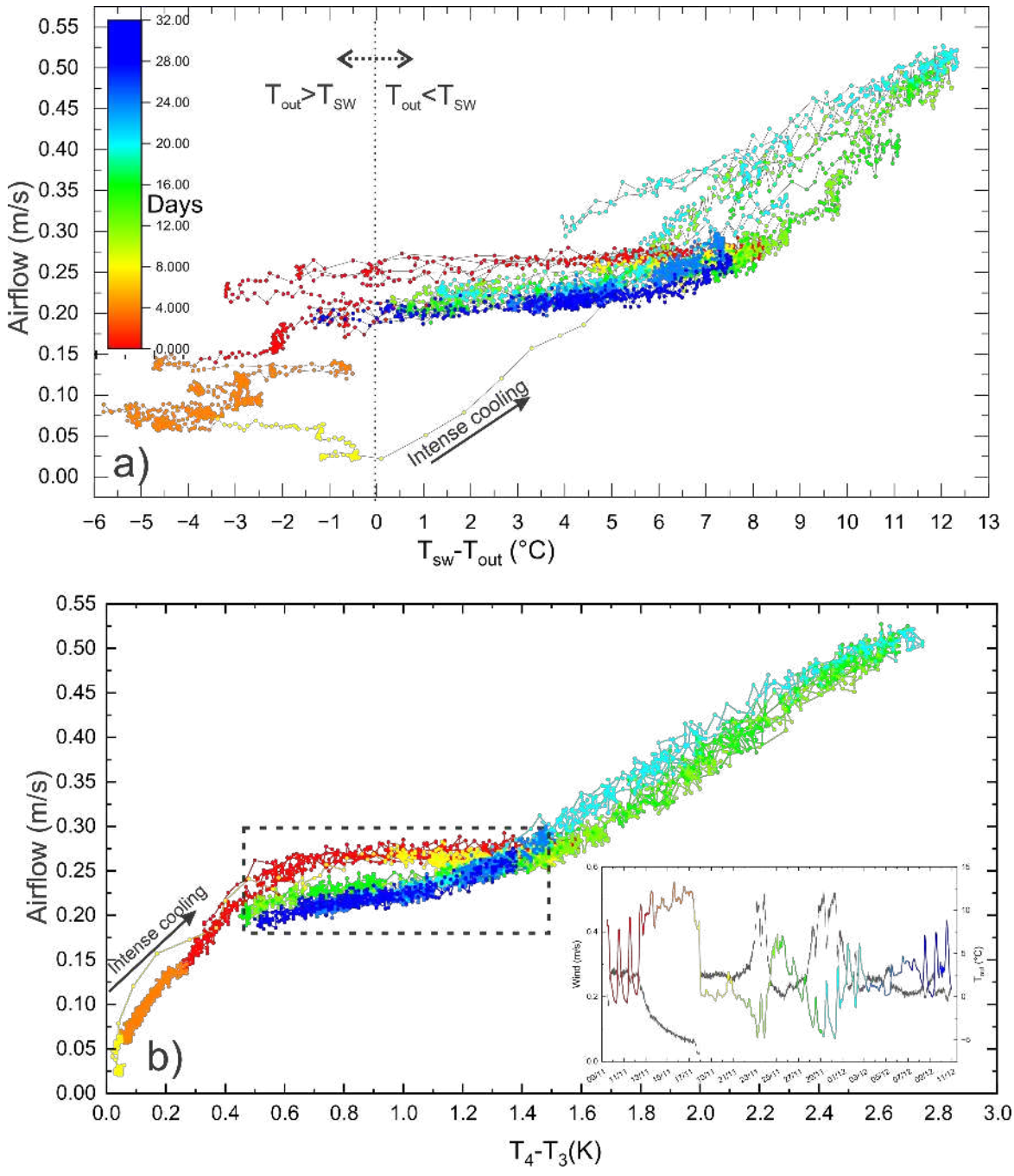


Fig. 7 Dependence of airflow velocity on temperature difference. a) Airflow velocity as a function of difference between switch temperature and external temperature. Colors denote the number of days since the beginning of observations (see also inset in Fig. 7b). b) Relation between airflow velocity and temperature

difference below the ceiling and above the floor (T_4-T_3). the color of each data point indicate the time elapsed since the start of the observations on 9 November (see the color scale and inset in Fig. 7b). The inset shows the time series of airflow velocity (black line) and external temperature, with the temperature plotted using the same color scale.

The drop in external temperature causes the instability that leads to intrusion of cold air. The airflow is driven by the density contrast between the descending cold-air layer (downflow) and the ascending warm-air layer (upflow), and is therefore a function of temperature difference between the two. This relationship is illustrated in Fig. 7b, which shows the dependence of airflow velocity on the temperature difference ($\Delta T = T4 - T3$) between the ceiling-level upflow (T4) and the floor-level downflow (T3) in the central part of the inclined passage (Fig. 2). The red—orange-yellow region before the rapid cooling shows the decay of airflow during the period with $T_{out}>T_{SW}$.

In the region highlighted by the rectangle in Fig, 7b, the airflow responds only weakly to increasing ΔT. Hereafter, we refer to this region as the velocity plateau.

As observed also for correlation with the outside temperatures (see Fig. 7a), the airflow in the early period (red) is slightly but distinctly stronger than in the latter periods (green, blue) for the same ΔT (Fig. 7b rectangle).

We can summarize the above presented observations as follows:

1. Starting from a stable situation, following a long period of external temperatures above the switch temperature (T_{sw}), with no measurable airflow and almost uniform temperature in the cave, the situation becomes unstable, when external air temperature drops below T_{sw}, and the buoyancy driven counterflow initiates.
2. The downward flow along the lower section of the main inclined passage continues along the main chamber and lower chamber and returns along the upper part of the passage cross-section as an upward flow towards the exit.
3. Temperature increases along the path in the downflow layer and decreases along the upflow, with fastest changes close to the entrance.
4. Temperature increases monotonically from the floor to the ceiling with smallest gradients in the middle, indicating most efficient mixing in the mixing layer.
5. When external temperature rises above T_{sw}, after a period of cold air intrusion(s) the airflow diminishes toward standstill and cave temperatures approach T_{sw}.

6. Airflow shows a nonuniform sigmoid relation to buoyancy with a clear plateau, or even a double-sigmoid behavior for the higher positioned anemometer.

We consider the temperature as the dominant factor influencing air density. Generally, there may be a situation in which variations in humidity or CO_2 concentration may play a role, but in the observations discussed here, we can safely consider the temperature as the dominant factor of air density differences (see Figure 2 in Gabrovšek 2023).

4.1 Seasonal evolution

Observations from autumn 2021 to summer 2022, revealed a similar pattern as shown in the Supplementary Information (Fig. S1). Fig. 8a gives a complete time series of airflow and ceiling minus floor temperatures which includes transition from winter to spring and summer. Fig. 8b shows the relation between ΔT and airflow velocity; triangles denote 10 min mean airflow velocities, while circles denote the corresponding 10 min maximum velocities. The relation is even more intriguing than the 2025 dataset; v_{max} increases with ΔT, and passes local maximum and minimum, until it rises again, but the increase is limited; v_{av} shows a plateau with less pronounced maximum. Colors denote the number of days since 24 October 2021, when the measurements started; this coincides with the beginning of cold air intrusions. Besides an intriguing general pattern with maximum and minimum, it also shows a clear seasonality pattern, when the airflow is stronger in the earlier part of cold season (red) than in the spring (green) for the same ΔT (Fig. 8b).

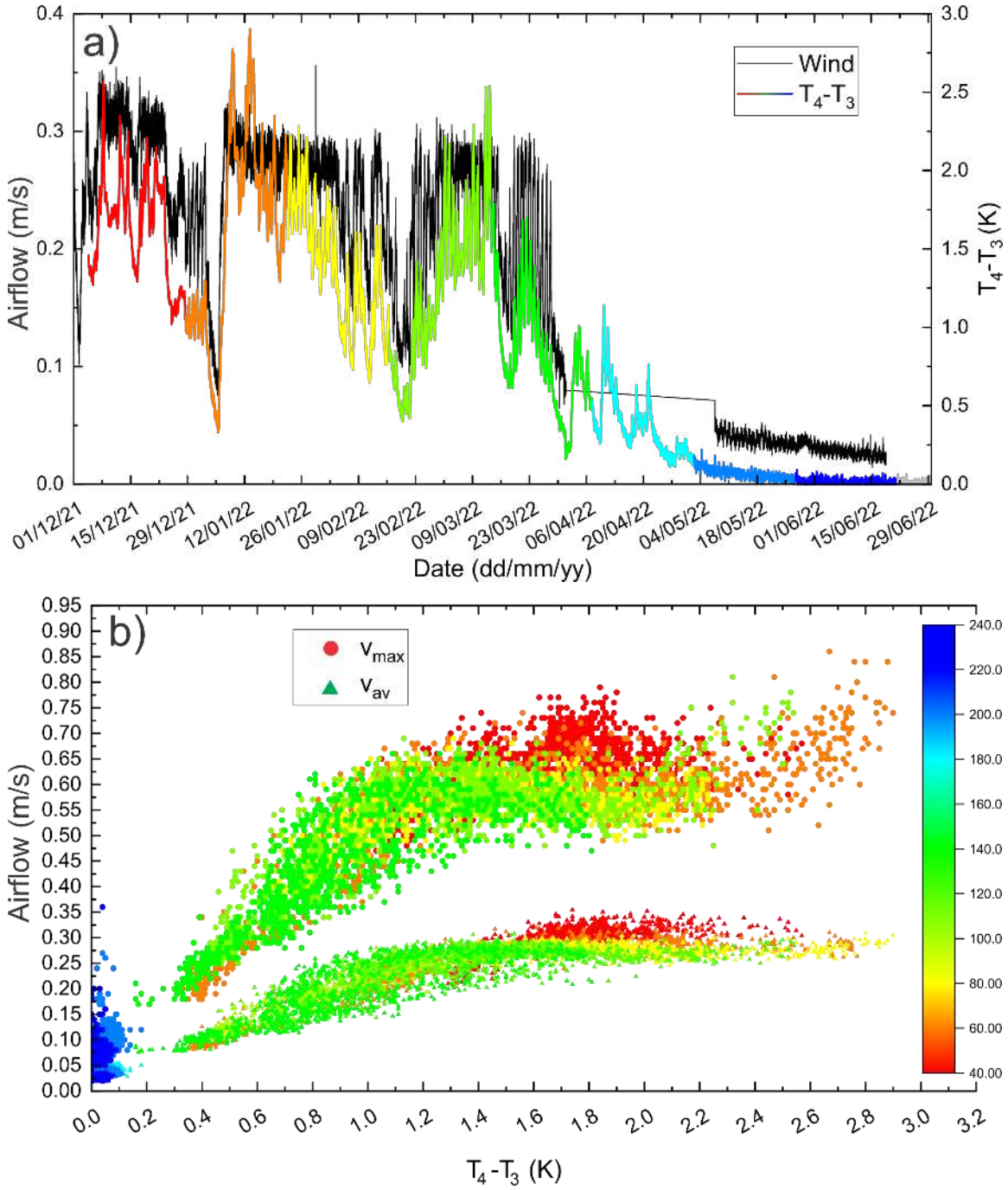


Fig. 8: a) Record of airflow velocity and T_4-T_3 between November 2021 and June 2022. Note that the anemometer was placed 75 cm above the floor. Colors denote days since the first observation (24 October 2021). b) Relation between T_4-T_3 and airflow velocity for 10 min average value of airflow velocity (triangles) and maximum airflow velocity in the 10 min interval (circles).

4.2 Properties and dynamics of stratified exchange flow

Intrusion of cold air replaces the cave air with the external air. During the observed rapid cooldown in November 17, 2025, which followed a warm period with external temperatures above T_{sw}, the initial phase of cold-air intrusion lasted about 80 minutes (Figs. 4, 5, 6, 9) and was followed by a relatively stable airflow. Prior to the cooling, the cave air temperatures were approaching T_{SW}, and the early stage of intrusion is dominated by the replacement of warm cave air with colder external air. Approximating the cave air volume as 5000 m^3, and using a representative layer-averaged velocity of 0.25 m/s, and a flow-layer cross-sectional area of 20 m^2 gives a one-way volume flux of approximately 5 m3/s and a nominal air-replacement timescale of approximately 17 min. The actual replacement time may be longer because of recirculation, incomplete mixing and weakly ventilated parts of the cave. In an adiabatic system, ventilation would cease once the internal air mass had been replaced by external air.

However, the buoyancy driving the counterflow is sustained by the heat exchange between the air and the surrounding rock and sediments. Two main processes can be envisaged: (a) heat exchange between the walls/sediments and the air, and (b) heat exchange between the counterflowing air layers.

Convective heat transfer between the rock/sediment and the air is proportional to their temperature difference. The heat exchange between the counterflowing layers and within them depends on the degree of mixing between and within the descending and ascending air layers. The observed system falls in the context of buoyancy-driven exchange flows in inclined ducts (Lefauve and Linden 2022; Meyer and Linden 2014). However, the cave system differs fundamentally from the classical exchange-flow configuration, when flow is exchanged along the sloping conduit between two infinite reservoirs with prescribed fluid densities. In our case the external atmosphere acts as an effectively infinite reservoir with prescribed properties, whereas the cave atmosphere constitutes a finite air volume whose density field evolves continuously through heat exchange with the surrounding rock and sediments. Consequently, the buoyancy driving the counterflow is continuously regenerated rather than prescribed.

The nearly continuous vertical temperature gradient (Fig. 6d) indicates turbulent mixing throughout both the upflowing and downflowing layers. The local reduction of the

temperature gradient in the interfacial region (around 1 m from the cave floor) suggests enhanced turbulent mixing there, consistent with an active interfacial shear layer between the counter-flowing streams. Kelvin–Helmholtz-type shear instabilities (Meyer and Linden 2014) may contribute to the initiation of mixing within the interfacial shear layer. The adjacent upflow and downflow contain turbulent eddies generated by wall shear, interfacial entrainment, and the turbulent energy cascade.

Using reasonable values for air viscosity ($\mu \approx (1.7 - 1.8) \times 10^{-5}$ Pa s), temperature differences of few K, the thermal expansion coefficient $\beta \approx (3.4\text{--}3.7) \times 10^{-3}$ K^{-1} and characteristic dimensions of the passage, the estimated Grashof numbers ($Gr \sim 10^9 - 10^{10}$) indicate that buoyancy forces greatly exceed viscous damping. The Reynolds numbers in the range $4\times10^4 - 10^5$ also indicate that the flow is fully turbulent.

The physical origin of the plateau in the $v(\Delta T)$ relationships shown in Figs. 7b and 8b remains uncertain. For each layer, the interfacial Froude number is defined as $Fr_i = |U_i|/\sqrt{g' h_i}$, where ($U_i$) and ($h_i$) are the layer-averaged velocity and layer thickness, respectively, and $g' = g\Delta\rho/\rho_0 \approx g\beta|\Delta T|$ is the reduced gravity. The hydraulic state of a two-layer exchange flow is determined by the composite Froude number $G = \sqrt{Fr_{lower}^2 + Fr_{upper}^2}$, with (G=1) representing the critical condition. With a crude assumtion that velocities and thicknesses of the two layers are equal ((U_{lower}=U_{upper}=v) and (h_{lower}=h_{upper}=1.5 m), the estimates in Tab. 1 give individual layer Froude numbers of (Fr_i=1.01–1.34) and composite values of G^2=2.03–3.61. These order-of-magnitude estimates indicate locally supercritical conditions at the measurement position rather than flow close to criticality.

However, the measured velocity is local rather than layer averaged, and the assumption of equal layer velocities and thicknesses is a simplification. Moreover, because the passage cross-section, layer thicknesses and interface position vary spatially, the hydraulic state may also change along the passage. A critical section with (G=1) may therefore occur at an unmonitored location and could migrate as the buoyancy forcing changes. Nevertheless, the plateau may also reflect changes in layer thickness and interface position, enhanced interlayer mixing and frictional dissipation, or movement of the interface relative to the fixed anemometer. The available measurements are insufficient to distinguish among these

mechanisms or to attribute the plateau conclusively to internal hydraulic control; confirmation would require simultaneous measurements of the depth-averaged velocities and thicknesses of both layers at several locations along the passage.

Table 1: Order-of-magnitude estimates of dimensionless numbers for selected temperature differences and airflow velocities relevant for the observations in Košelevka. Gr = Grashof number; Re = Reynolds number; and squared composite Froude number G^2.

ΔT (K)	U (m/s)	Gr	Re	Fr_{lower}	G^2
0.50	0.20	2×10^9	4×10^4	1.25	3.11
1.00	0.25	4×10^9	5×10^4	1.10	2.43
1.50	0.28	6×10^9	5.5×10^4	1.01	2.03
2.00	0.38	8×10^9	7.6×10^4	1.18	2.80
2.80	0.51	1.1×10^{10}	1×10^5	1.34	3.61

The ceiling-level upflow cools along the passage, including in its inner part, rather than only near the entrance (Fig. 5,b,d). Away from the entrance, the thermally buffered cave rock is expected to be warmer than the winter airflow; consequently, air–rock heat exchange should warm rather than cool the upflow. The observed cooling is therefore more consistent with heat exchange or mixing between the warmer upflow and the colder downflow. Nevertheless, because rock-surface temperatures were not measured, a contribution from air–rock heat exchange cannot be completely excluded.

4.3 Thermal inertia and equilibration to steady state

As observed above in Figs. 4–5, when the external temperature rises above T_{sw} after a period of cold air intrusion the system equilibrates to a stable state with “almost” uniform temperature and negligible airflow; details are shown on Fig. 9.

During cold-air intrusion, the airflow cools the sediments and cave walls, producing a nonuniform spatial distribution of rock and sediment temperature. Floor temperatures are lower than ceiling temperatures and increase from the entrance toward the main and lower chambers. This disequilibrium drives the counterflow independently of the external temperature, as seen on Fig. 7, where airflow becomes uncorrelated with external

temperature, but remains a function of ΔT. The counterflow is sustained until the temperature field within the cave equilibrates.

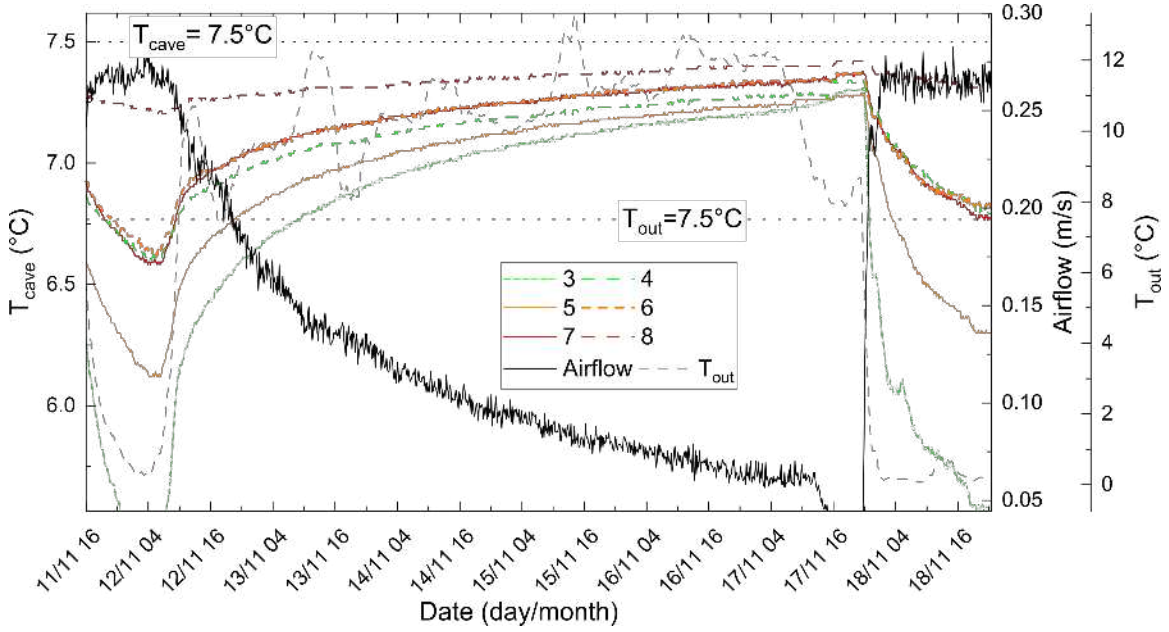


Fig. 9: Airflow velocity, cave and external temperature during equilibration, when T_{out}>7.5°C.

4.4 On thermal length scale and seasonal evolution of airflow

Cooling of the sediment–rock layer surrounding the void has several consequences. As shown by Gabrovšek (2023), cooling of the walls promotes deeper penetration of cold air into the cave. In a simple situation with a straight tube connecting two entrances at different elevations, cooling of the walls reduces buoyancy because it allows cold air to penetrate deeper into the passage, thereby reducing the density contrast between the warmer cave air and the colder external air (Fig. 10a, case 1). In a V-shaped passage (Fig. 10a, case 2), which is a closer analogue to the present case, the situation is more complex. Here, buoyancy increases with penetration length because it depends on the thermal disequilibrium between the inflow and outflow limbs. As cold air penetrates deeper, this disequilibrium grows until a new equilibrium is established between airflow velocity, penetration length, and buoyancy forcing. Under counter-flow conditions (Fig. 10a, case 3), additional complications arise from heat exchange between and within the counterflowing air masses. The magnitude of this exchange depends on the flow regime and on the thickness of the mixing layer separating the two flows.

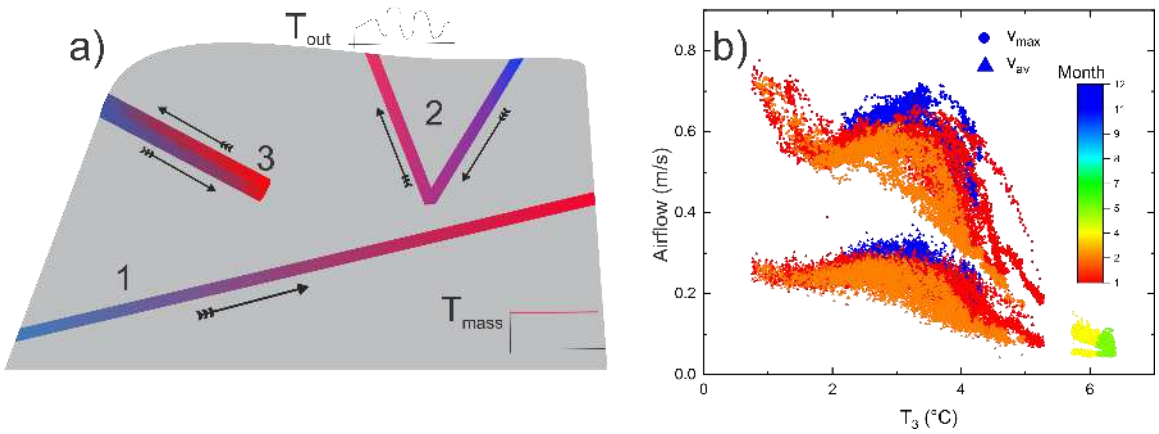


Fig. 10: (a) Conceptual comparison of winter ventilation in (1) a straight passage connecting entrances at different elevations, (2) a V-shaped passage, and (3) a single-entrance cave with counterflow. (b) Airflow velocity (10 min average (triangles) and 10 min maximum (circles) as a function of near-floor temperature T_3 during the 2021/2022 season. Colors indicate the month of the year.

To illustrate the seasonal evolution of the airflow, Fig. 10b shows the relationship between the near-floor temperature (T_3) and airflow velocity. During the later part of the cold season (February-March; Fig. 10b, orange), the same near-floor temperature is attained at lower airflow velocities than earlier in the season (December; Fig. 10b, blue). This indicates that, as the surrounding rock cools over the winter, the incoming cold air is warmed less efficiently along its flow path, allowing it to penetrate farther into the cave.

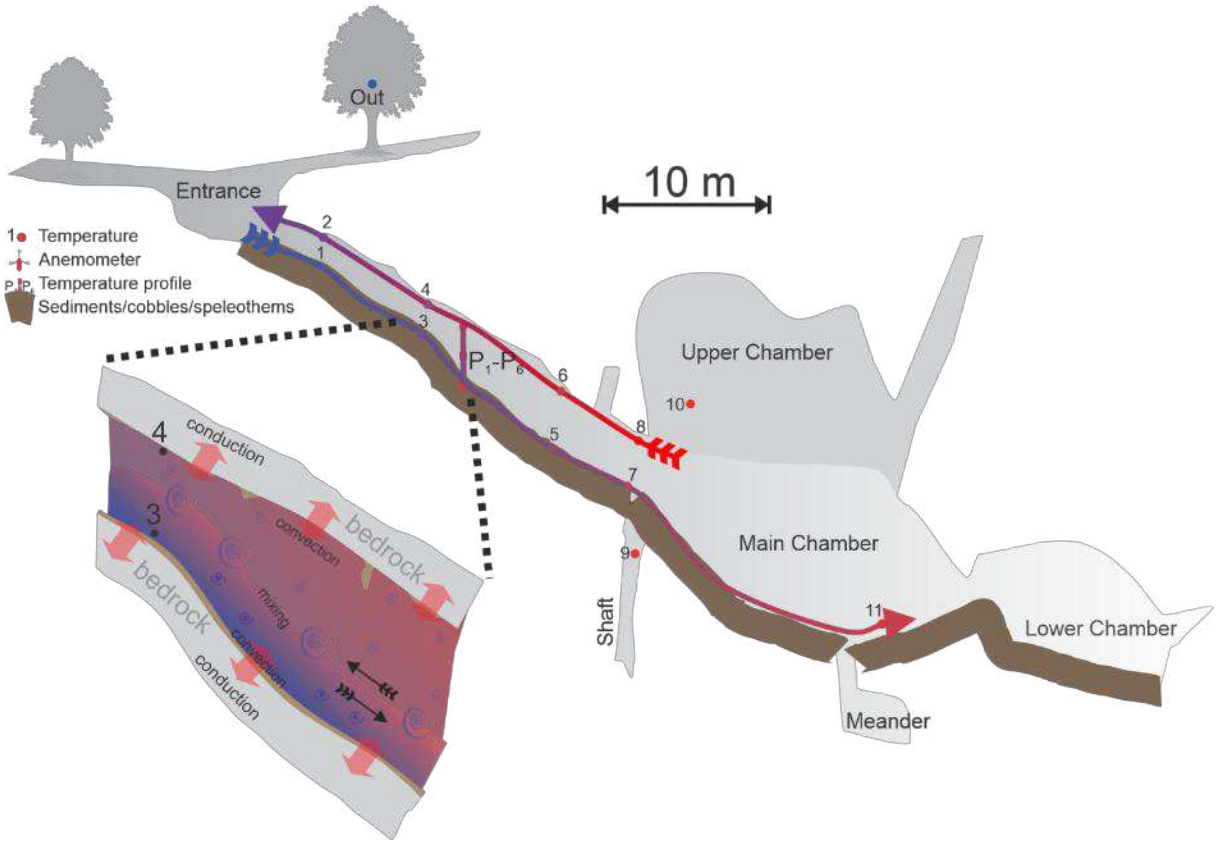


Fig. 11 Extended cross-section of Koševelka Cave with colors showing a qualitative temperature profile along the airflow. Arrows indicate airflow direction; temperature is presented on a blue–red colour scale. Excerpt shows a section of the main passage with (qualitative) temperature distribution and heat exchange mechanisms.

5 Conclusions

We present and discuss results from a relatively simple cave, where buoyancy drives a two-layered flow along an inclined passage. Within the cave, the density field evolves continuously owing to heat exchange between the air and the surrounding rock and sediments. Consequently, the airflow, heat transfer, and buoyancy become dynamically coupled. The results also indicate heat exchange between the upflowing and downflowing air layers, as well as within each layer. The processes are summarized in Fig. 11.

The measured relationship between buoyancy proxies and airflow velocity exhibits a sigmoid behaviour. The estimated Grashof and Reynolds numbers identify the ventilation

as a buoyancy-dominated turbulent exchange flow. Assuming equal layer-averaged velocities and layer thicknesses of 1.5 m, composite Froude numbers of (G=1.42–1.90) indicate locally supercritical flow at the measurement position but do not determine the hydraulic state throughout the passage. The velocity plateau may reflect a migrating critical section at an unmonitored location or changes in layer geometry, interlayer mixing, frictional dissipation, and interface position relative to the fixed anemometer.

When the external temperature rises above the switch temperature—the temperature at which the external air is approximately in thermal equilibrium with the rock massif—cave temperatures are no longer directly influenced by external conditions. However, owing to the thermal inertia of the surrounding rock and sediments, the temperature disequilibrium between the floor and ceiling continues to drive airflow until thermal equilibrium within the cave is reached.

In this work, we limit ourselves to a qualitative description of the observations and highlight the underlying physical mechanisms. Nevertheless, the results demonstrate the richness of processes that can arise even in a relatively simple geometry. They also illustrate how thermal inertia, buoyancy, and turbulent mixing interact to govern natural ventilation in confined subsurface environments.

Several open questions remain and require more detailed investigation. The flow structure across individual cave cross-sections could be examined using laser-sheet visualization and particle image velocimetry. Additional temperature measurements within the surrounding rock and cave sediments would improve understanding of the thermal coupling between the different media. Ultimately, the goal is to develop a quantitative model capable of reproducing the observed flow and heat-transfer dynamics.

Although this study focuses on a single cave, similar ventilation patterns likely occur in other karst systems but remain poorly documented. The identified ventilation regime provides a straightforward explanation for the apparent bimodal CO_2 distribution (Supplementary Fig. S2). These processes are also relevant to cave-ice dynamics in ice caves.

We hope that the observations presented here will stimulate further field, experimental, and modelling studies and contribute to a more general understanding of natural ventilation and subsurface climate dynamics.

Acknowledgements The authors acknowledge the financial support from the as a part of the CARDICARST project, funded by Slovenian Research Agency (J7-4630) and the Croatian Science Foundation (IPS-2022-02), and by the project "Exploring the potential of moonmilk speleothems as archives of palaeo-environmental information", funded by the Slovenian Research Agency (J1-50028).

References

Armi L (1986) The hydraulics of two flowing layers with different densities. J Fluid Mech 163:27–58. https://doi.org/10.1017/S0022112086002197

Badino G (1995) Fisica del Clima Sotterraneo. Instituto Italiano di Speleologia, Bologna

Borsato A, Frisia S, Jones B, van der Borg K (2000) Calcite Moonmilk: Crystal Morphology and Environment of Formation in Caves in the Italian Alps. J Sediment Res

Buzjak N, Gabrovšek F, Perşoiu A, et al (2024) CO2 Emission from Caves by Temperature-Driven Air Circulation—Insights from Samograd Cave, Croatia. Climate 12:199. https://doi.org/10.3390/cli12120199

Covington MD, Luhmann AJ, Wicks CM, Saar MO (2012) Process length scales and longitudinal damping in karst conduits. J Geophys Res Earth Surf 117:2011JF002212. https://doi.org/10.1029/2011JF002212

Ford DC, Williams P (2007) Karst Hydrogeology and Geomorphology. John Wiley & Sons, Chichester

Ford JD, Cullingford CHD (eds) (1976) The physics of caves. In: The Science of Speleology. Academic Press, London, pp 329–58

Gabrovšek F (2023) How do caves breathe: The airflow patterns in karst underground. PLOS ONE 18:e0283767. https://doi.org/10.1371/journal.pone.0283767

Gabrovsek F (2026) Koševelka Cave Meteo Data. https://zenodo.org/doi/10.5281/zenodo.21624121

Ghezzi D, Jiménez-Morillo NT, Foschi L, et al (2024) The microbiota characterizing huge carbonatic moonmilk structures and its correlation with preserved organic matter. Environ Microbiome 19:25. https://doi.org/10.1186/s40793-024-00562-9

Kowalczk AJ, Froelich PN (2010) Cave air ventilation and CO2 outgassing by radon-222 modeling: How fast do caves breathe? Earth Planet Sci Lett 289:209–219. https://doi.org/10.1016/j.epsl.2009.11.010

Kukuljan L, Gabrovšek F, Covington MD, Johnston VE (2021) CO2 dynamics and heterogeneity in a cave atmosphere: role of ventilation patterns and airflow pathways. Theor Appl Climatol. https://doi.org/10.1007/s00704-021-03722-w

559 Lacanette D, Bassel L, Salmon F, et al (2023) Climate of a cave laboratory representative for rock art caves
560 in the Vézère area (south-west France). Int J Speleol 52:85–100. https://doi.org/10.5038/1827-
561 806X.52.2.2442
562 Lefauve A, Linden PF (2022) Buoyancy-Driven Exchange Flows in Inclined Ducts. J Fluid Mech 937:A34.
563 https://doi.org/10.1017/jfm.2022.115
564 Linden PF (1999) The Fluid Mechanics of Natural Ventilation. Annu Rev Fluid Mech 31:201–238.
565 https://doi.org/10.1146/annurev.fluid.31.1.201
566 Lismonde B (2002) Climatologie du Monde Souterrain. Departemental de speleologie Iser, Isere
567 Luetscher M, Jeannin P-Y, Haeberli W (2005) Ice Caves as an Indicator of Winter Climate Evolution: A
568 Case Study from the Jura Mountains. Theor Appl Climatol 82:187–205.
569 https://doi.org/10.1007/s00704-005-0123-0
570 Luetscher M, Lismonde B, Jeannin P-Y (2008) Heat exchanges in the heterothermic zone of a karst system:
571 Monlesi cave, Swiss Jura Mountains. J Geophys Res 113:F02025.
572 https://doi.org/10.1029/2007JF000892
573 Luhmann AJ, Covington MD, Myre JM, et al (2015) Thermal damping and retardation in karst conduits.
574 Hydrol Earth Syst Sci 19:137–157. https://doi.org/10.5194/hess-19-137-2015
575 Meyer CR, Linden PF (2014) Stratified Inclined Duct Flows. J Fluid Mech 753:242–253.
576 https://doi.org/10.1017/jfm.2014.376
577 Mihevc A (2018) Prostorski razpored in časovni potek temperatur v Potočki zijalki na Olševi - osnova za
578 razumevanje morfologije jamskih tal. Raziskave Področja Geod. Geofiz.
579 Mihevc A (2021) Ice in caves and its effect on thermal inversion and permafrost in the case of the Velika
580 ledena jama v Paradani, Smrekova draga and neighbouring dolines. Acta Carsologica 50:.
581 https://doi.org/10.3986/ac.v50i2-3.10495
582 Miller AZ, Garcia-Sanchez AM, Martin-Sanchez PM, et al (2018) Origin of abundant moonmilk deposits
583 in a subsurface granitic environment. Sedimentology 65:1482–1503. https://doi.org/10.1111/sed.12431
584 Palmer AN (2007) Cave geology. Cave Books, Dayton, Ohio
585 Perşoiu A (2018) Chapter 3 - Ice Caves Climate. In: Perşoiu A, Lauritzen S-E (eds) Ice Caves. Elsevier, pp
586 21–32
587 Ravbar N, Kosutnik J (2014) Variations of karst underground air temperature induced by various factors
588 (Cave of Županova jama, Central Slovenia). Theor Appl Climatol 116:327–341.
589 https://doi.org/10.1007/s00704-013-0955-4
590 Šebela S, Turk J (2018) Črna Jama as a cold air trap cave within Postojna Cave, Slovenia. Theor Appl
591 Climatol 134:741–751. https://doi.org/10.1007/s00704-017-2304-5
592 Spotl C, Fairchild I, Tooth A (2005) Cave air control on dripwater geochemistry, Obir Caves (Austria):
593 Implications for speleothem deposition in dynamically ventilated caves. Geochim Cosmochim ACTA
594 69:2451–2468
595

Supplementary Files

This is a list of supplementary files associated with this preprint. Click to download.

- SupplementaryInformation.docx